Global Biogeochemical Cycles

RESEARCH ARTICLE
10.1029/2018GB006026

Hydrologic Controls of Methane Dynamics in Karst Subterranean Estuaries

D. Brankovits[1,2,3], J. W. Pohlman[1,4], N. K. Ganju[4], T. M. Iliffe[1], N. Lowell[5], E. Roth[6], S. P. Sylva[7], J. A. Emmert[8], and L. L. Lapham[9]

[1]Department of Marine Biology, Texas A&M University at Galveston, Galveston, TX, USA, [2]Now at Woods Hole Coastal and Marine Science Center, U.S. Geological Survey, Woods Hole, MA, USA, [3]Now at Department of Marine Chemistry and Geochemistry, Woods Hole Oceanographic Institution, Woods Hole, MA, USA, [4]Woods Hole Coastal and Marine Science Center, U.S. Geological Survey, Woods Hole, MA, USA, [5]Lowell Instruments, North Falmouth, MA, USA, [6]Onset Computer Corporation, Bourne, MA, USA, [7]Department of Marine Chemistry and Geochemistry, Woods Hole Oceanographic Institution, Woods Hole, MA, USA, [8]Moody Gardens Aquarium, Galveston, TX, USA, [9]Chesapeake Biological Laboratory, University of Maryland Center for Environmental Science, Solomons, MD, USA

Key Points:
- Concurrent meteorological, hydrological, and chemical records are used to study sources and sinks of methane in a karst subterranean estuary
- Increased precipitation enhances methane oxidation by mixing anoxic methane-rich waters with oxygenated waters
- A hydrologically based mass balance model provides a first-order estimate for the magnitude of the methane sink within the catchment region

Supporting Information:
- Supporting Information S1

Correspondence to:
D. Brankovits and J. W. Pohlman,
dbrankovits@whoi.edu;
jpohlman@usgs.gov

Citation:
Brankovits, D., Pohlman, J. W., Ganju, N. K., Iliffe, T. M., Lowell, N., Roth, E., et al. (2018). Hydrologic controls of methane dynamics in karst subterranean estuaries. *Global Biogeochemical Cycles*, *32*, 1759–1775. https://doi.org/10.1029/2018GB006026

Received 10 JUL 2018
Accepted 2 OCT 2018
Accepted article online 9 NOV 2018
Published online 7 DEC 2018

Abstract Karst subterranean estuaries (KSEs) extend into carbonate platforms along 12% of all coastlines. A recent study has shown that microbial methane (CH_4) consumption is an important component of the carbon cycle and food web dynamics within flooded caves that permeate KSEs. In this study, we obtained high-resolution (~2.5-day) temporal records of dissolved methane concentrations and its stable isotopic content ($\delta^{13}C$) to evaluate how regional meteorology and hydrology control methane dynamics in KSEs. Our records show that less methane was present in the anoxic fresh water during the wet season (4,361 ± 89 nM) than during the dry season (5,949 ± 132 nM), suggesting that the wet season hydrologic regime enhances mixing of methane and other constituents into the underlying brackish water. The $\delta^{13}C$ of the methane (−38.1 ± 1.7‰) in the brackish water was consistently more ^{13}C-enriched than fresh water methane (−65.4 ± 0.4‰), implying persistent methane oxidation in the cave. Using a hydrologically based mass balance model, we calculate that methane consumption in the KSE was 21–28 mg $CH_4 \cdot m^{-2} \cdot year^{-1}$ during the 6-month dry period, which equates to ~1.4 t of methane consumed within the 102- to 138-km^2 catchment basin for the cave. Unless wet season methane consumption is much greater, the magnitude of methane oxidized within KSEs is not likely to affect the global methane budget. However, our estimates constrain the contribution of a critical resource for this widely distributed subterranean ecosystem.

Plain Language Summary Subterranean estuaries occur worldwide where fresh and marine-derived waters mix within coastal aquifers, creating a chemical reaction zone that alters the composition of materials transported to the sea. According to a recent study, methane—a potent greenhouse gas—and the bacteria that feed on it form the basis of a complex food web restricted to cave networks flooded by the subterranean estuary. Questions about the seasonality and magnitude of this methane sink remain unclear. Unprecedented chemical records collected during this study with simultaneous meteorological and hydrological data reveal that methane accumulation is significantly greater during the dry season than during the wet season when rainfall is more prevalent and greater mixing in the coastal aquifer facilitates methane consumption. We estimate that ~1.4 t of methane are consumed during a 6-month-long dry period within the ~100-km^2 catchment region. This estimate constrains the contribution of a critical energy source for karst subterranean estuary ecosystems.

1. Introduction

Subterranean estuaries occur globally beneath carbonate, siliciclastic, and basaltic coastlines where mixing of meteoric fresh water and marine-derived groundwater creates a biogeochemical reaction zone that supports a subterranean ecosystem (Bishop et al., 2015; Brankovits et al., 2017) and alters the chemical composition of submarine groundwater discharge (Moore, 1999, 2010). Multiple studies suggest that submarine groundwater discharge is the dominant source of dissolved terrestrial material, including nutrients, carbon, and trace metals, to the oceans (Kwon et al., 2014; Lee et al., 2010; Taniguchi et al., 2002). Carbonate and basaltic subterranean estuaries are distinct from those in siliciclastic coastlines because they contain cave passages that enhance hydraulic transport and exchange of material with the coastal ocean (Beddows

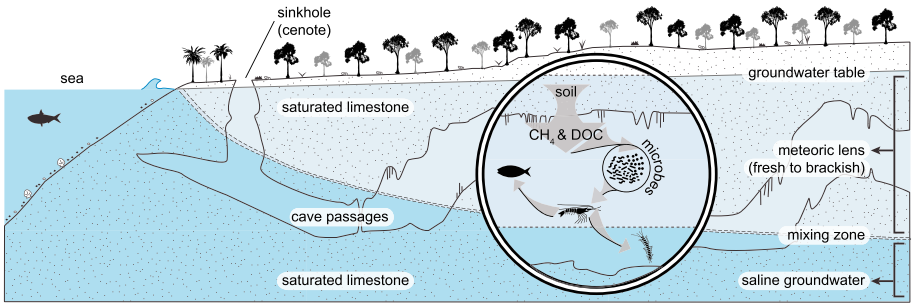

Figure 1. Unconfined coastal carbonate aquifer with cave passages that provide access to the karst subterranean estuary. Density stratification separates fresh, brackish, and saline water masses separated by sharp mixing zones (haloclines). Direct interconnections between processes related to meteorology, coastal oceanography, and geology shape the hydrological setting of the karst subterranean estuary. A subterranean microbial loop (inset circle) transfers dissolved organic matter formed by decomposition of terrestrial vegetation into the *anchialine* food web (Brankovits et al., 2017). DOC = dissolved organic carbon; CH_4 = methane.

et al., 2007; Martin et al., 2012; Perry et al., 2002). Therefore, cave networks profoundly influence the condition of groundwater resources (Bauer-Gottwein et al., 2011; Vesper et al., 2001) and ecosystems that reside within them (Brankovits et al., 2017; Pohlman, 2011), as well as the chemical composition of submarine groundwater discharge (Gonneea et al., 2014). Karstic (solutionally eroded carbonate) platforms account for at least ~12% of all submarine groundwater discharge (Ford & Williams, 2013; Gonneea et al., 2014). Thus, biogeochemical processes occurring within *karst subterranean estuaries* (KSEs) are likely to impact coastal ocean carbon budgets on a global scale.

Interconnections between the hydrogeology, meteorology, and coastal oceanography associated with unconfined coastal carbonate aquifers (Figure 1) control the structure of the meteoric lens and distribution of dissolved materials in KSEs (Beddows et al., 2007; Coutino et al., 2017; Kovacs et al., 2017; Martin et al., 2012). Vertically segregated density interfaces (pycnoclines) maintained by thermal and salinity gradients isolate electron-rich, energy-yielding organic compounds, for example, dissolved organic matter (DOM) and methane, from electron accepting agents of cellular respiration (e.g., sulfate and oxygen; Pohlman, 2011). Enhanced flow within cave conduits distributes and mixes these life-sustaining materials within the KSE. For example, oxygen enters the aquifer through point recharge of meteoric water (Ford & Williams, 2013), while the tidal-pumping of coastal seawater (Beddows et al., 2007; Martin et al., 2012) introduces dissolved oxygen and sulfate that are respectively available for aerobic and anaerobic microbes (Socki et al., 2002). Seasonal precipitation patterns and extreme meteorological events (e.g., hurricanes) can alter the physical distribution and mixing of material within the caves (Coutino et al., 2017; Kovacs et al., 2017) with corresponding effects on the cave ecology and transformation of material expelled into the coastal ocean.

A recent investigation of a KSE in the Yucatan Peninsula (Mexico) found that the meteoric lens in some domed cave passages contains a thin (20–60 cm) mixing zone that separates shallow and fresh ($<$ 0.3 psu) water from an underlying layer of brackish (~1.8 psu) water (Brankovits et al., 2017). The fresh water (FW) is anoxic and contains high concentrations of DOM (including methane) formed from degraded plant matter, while the brackish water (BW) is hypoxic and contains lesser quantities of DOM, with methane showing clear evidence of microbial oxidation. Evidence that methane-consuming bacteria (methanotrophs) and other DOM consuming microbes are present in the environment, with lipid biomarkers from these microbes present in the tissue of filter-feeding shrimp, suggests DOM is the base of the food web. The authors calculate that, on average, methane carbon produced chemoautotrophically in the KSE comprises 21% of the biomass of cave-adapted shrimp species capable of feeding on the bacteria. These findings and the observation that suspended particulate organic matter is scant supports the hypothesis that globally dispersed ecosystems in KSEs, also referred to as *anchialine* ecosystems (Bishop et al., 2015; Iliffe & Kornicker, 2009), subsist primarily on DOM (Brankovits et al., 2017; Pohlman, 2011).

In addition to being a nutritive source for aquatic ecosystems (e.g., Bastviken et al., 2003; He et al., 2015; Levin, 2005; Niemann et al., 2013), methane accounts for ~20% of greenhouse gas radiative forcing in the atmosphere (Intergovernmental Panel on Climate Change, 2014). In the natural environment, methane (CH_4) is

primarily produced by methanogenic Archaea in organic matter rich anoxic sediments (e.g., Bastviken et al., 2004). Methanotrophy (microbial methane oxidation) is an important mechanism that limits methane emissions to the atmosphere. For example, perhaps 90% of the ~85 Tg CH_4/year produced globally in anoxic marine and freshwater systems is consumed by anaerobic and aerobic methanotrophs before reaching the atmosphere (Reeburgh, 2007). These pathways limit natural methane contributions to the global atmosphere to ~2–10% from lakes (Bastviken et al., 2004) and no more than 2% from oceans (Reeburgh, 2007). However, far less is known about the balance of methane production and consumption in subterranean estuaries. A recent study suggests that more than 80% of the methane produced in anoxic groundwater within a barrier island subterranean estuary was oxidized by anaerobic methanotrophy prior to its expulsion into the coastal ocean (Schutte et al., 2016). In KSEs, as much as 93% of the methane introduced into the caves is oxidized (Brankovits et al., 2017); however, the magnitude of the methane sink and the hydrological mechanisms that regulate its availability and utilization are unknown.

In this study, continuous (6–12 month) chemical and hydrological records identify how external environmental controls and the groundwater hydrology affect the concentrations and consumption of methane within caves of a KSE in the Yucatan Peninsula, Mexico. Precipitation and barometric pressure were monitored above ground, while water level, flow velocity, and water temperature were measured below ground. Osmotic pumps collected water samples to be measured for salinity and methane concentrations every ~2.5 days, as well as for δ^{13}C-CH_4 periodically from the methane-rich FW and the relatively methane-depleted BW. With these data, we quantify the magnitude of methane consumed within the catchment basin of a major cave conduit during a dry season and provide a generic model for relationships between groundwater hydrology, local meteorology, coastal oceanography, and ecosystem function within terrestrially influenced KSEs.

2. Methods

2.1. Study Site

The study site is located in the Caribbean coast of the Yucatan Peninsula (Quintana Roo, Mexico; Figure 2a) where the permeable limestone platform is characterized by relatively flat topography and an absence of surface flowing streams and rivers (Beddows et al., 2007; Perry et al., 2002). The area is subject to rapid development and urbanization, primarily due to tourism, which threatens native ecosystems, including offshore coral reefs, coastal mangroves, seagrasses, the inland dry tropical forest, as well as ground water resources and groundwater-dependent habitats. (Bauer-Gottwein et al., 2011). In this region, the Holbox Fracture Zone and Xel Ha Zone (Perry et al., 2002) contains more than 1,000 km of mapped cave conduits (Kambesis & Coke, 2013) that provide direct access to the inland portion of the subterranean estuary over an area (~1,100 km^2) comparable to large surface estuaries.

The research site is located in a region of seasonally dry tropical climate with dry (typically from December to April/May) and wet (from May to November) seasons (Curtis et al., 1996; Kottek et al., 2006). About 250 mm ($<$ 20%) of the mean annual rainfall of ~1,500 mm occurs during the dry season, with maximum rainfall occurring during the months of June and September (Curtis et al., 1996; Kottek et al., 2006; Peel et al., 2007). Because there is no surface runoff, all precipitation that is not evaporated or transpired recharges the aquifer (Gondwe et al., 2010). Akin to streams and tributaries that define a river basin watershed, upstream conduits that feed large cave passages define the catchment basin of a KSE.

The sampling stations within the caves were accessed by scuba diving through a flooded sinkhole (locally referred to as cenote) called Cenote Bang (20°12.62′N, 87°30.06′W), located beneath a dry tropical forest 6.6 km from the coastline near the town of Tulum (Figure 2b). The water column is characterized by two sharp haloclines (named as H1 and H2 in Figure 2c; Brankovits et al., 2017). The meteoric lens consists of a FW (~0.2 psu) and a BW (~1.8 psu) layer. The FW largely resides within the rock matrix. The BW between the FW and the deeper saline groundwater (SG; $>$ 30.0 psu) occupies the largest fraction of the cave passages. A halocline separates the FW and BW at about 4 m below the groundwater table (H1), and a second interface separates the BW and SG at about 20 m below the groundwater table (H2). For simplicity, the three hydrologic regimes defined by Brankovits et al. (2017) as MFW, MBW, and SGW are hereby changed to FW, BW, and SG.

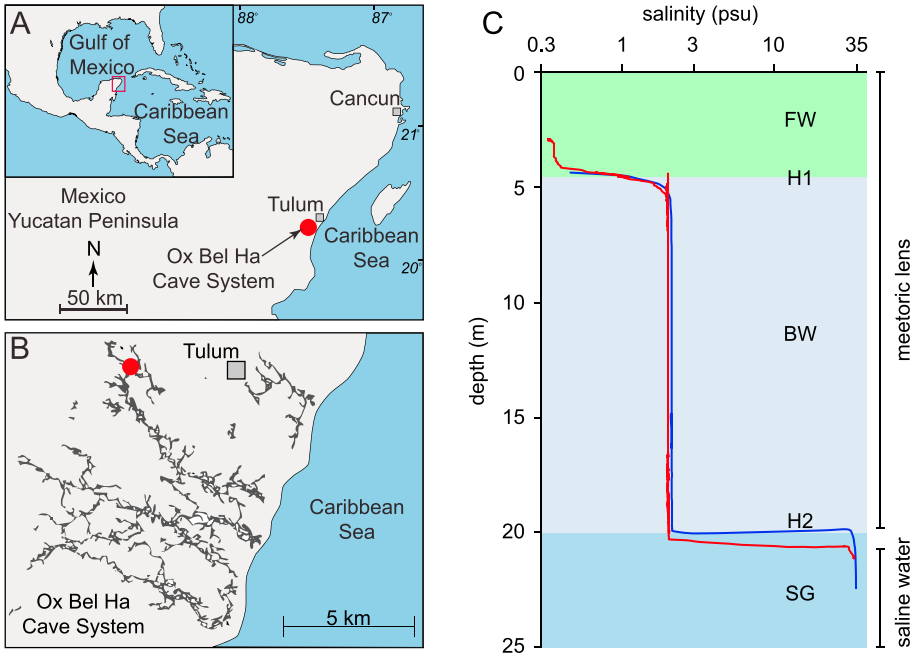

Figure 2. Study site and salinity profiles. (a) The study site is located within the Ox Bel Ha cave system in the northeastern Yucatan Peninsula, which separates the Caribbean Sea from the Gulf of Mexico. (b) The Ox Bel Ha cave system consists of more than 240 km of mapped underwater cave conduits. (c) A salinity profile of the karst subterranean estuary investigated in this study (data from Brankovits et al., 2017) includes two sharp haloclines (H1, shallow, and H2, deep) that partition the water column into three distinct water masses (fresh water, FW; brackish water, BW; saline groundwater, SG) accessible via cave passages.

2.2. Environmental Parameters

Monitoring devices were installed on the surface and in the cave environment (Figure S1 in the supporting information). A meteorological station located 3.5 km from the study site measured precipitation, barometric pressure, and air temperature between 18 January 2015 and 22 January 2016. The station was placed on the rooftop at a secure site (Speleotech facility; 20°12.396′N 87°28.079′W) about 15 m above ground level and well above the forest canopy in the town of Tulum, Quintana Roo. Precipitation was measured with a rain gauge (Onset RG-3, calibration accuracy of ±1.0%, up to 2 cm/hr; 0.2-mm resolution; time accuracy ±1 min per month) and is presented as daily total precipitation (mm/day). Barometric pressure was monitored at 15-min time intervals alongside the rain gauge with an Onset U20 data logger ($<$ 0.02-kPa resolution and a ±0.3% FS or 0.62 kPa accuracy as the maximum error) that also measured air temperature (0.1 °C resolution, ± 0.44 °C accuracy).

Within the cave, groundwater flow velocity, water level, and water temperature were monitored at 17-m water depth in the BW and at 22-m water depth in the SG. Velocity was measured as current speed and direction with a TCM-1 (Lowell Instruments, LLC) tilt current meter (TCM; ± 2 cm/s + 3% of reading accuracy and 0.1-cm/s resolution; bearing ±5° accuracy for speed $>$5 cm/s^{-} with a 0.1° resolution) at 1-min intervals (Lowell et al., 2015). Water level measured with an Onset U20 logger (± 0.21 cm with an error less than ±1.0 cm at 15-min intervals) is reported as the departure from the mean value after compensating for barometric pressure changes measured at the meteorological station. The FW was only accessible within dome-like features of the cave ceiling at depths shallower than 4 m. Based on the geomorphically protected nature of these domes, we assume negligible water flow, and we were unable to deploy the TCM.

2.3. Chemical Records

Continuous water samples for analysis of salinity, methane concentration, and $\delta^{13}C$ of methane were obtained with OsmoSamplers (OSs). OSs have been used to track temporal changes in methane concentrations in a variety of settings, including eutrophic estuaries (Gelesh et al., 2016) and hydrocarbon seeps in the deep ocean (Lapham et al., 2008, 2013; Wilson et al., 2015). For this study, each OS had eight semipermeable

membranes (2ML1, Durect Co.) that separated a saturated salt solution from deionized water. The resultant osmotic potential between the chambers allows water to diffuse across the membranes (Jannasch et al., 2004) and resulted in pumping rates ranging from 0.76 to 1.24 ml/day for the OSs between deployments in the BW and FW. Water emitted from the reservoir is replaced by degassed deionized water from within a ~300-m coil of 1.59 mm outer diameter gas-impermeable copper tubing, which is balanced by drawing water from the environment through a 0.2-μm hydrophilic filter (Rhizosphere Research Products) at the other end of the coil.

OSs were deployed following protocols developed by Lapham et al. (2008) with modifications for scuba diver deployment. The pump and the sample coil were packed in a plastic laundry basket in a compact and streamlined manner allowing the diver to manually transport and deploy the device. The sample inlet of the FW-OS was placed in the FW at 3.5-m water depth, above the shallow halocline (H1), near the cave ceiling. The inlet port of the BW-OS was placed at 7.5 m, below the shallow halocline, in the BW. OSs were codeployed in two subsequent time periods to cover the wet and dry seasons. The deployment periods were from 17 January to 14 June 2015. The second deployment was from 19 June 2015 to 20 January 2016. Upon recovery, the coils were sealed on either end and stored at ~7 °C in the field, transported to the United States and stored at 4 °C until they were subsampled in the laboratory within 2 months of collection.

Subsampling followed details in Gelesh et al. (2016) and included crimping 4.5-m sections of the copper tubing that were later split into a 4-m-long section, containing water for analysis of methane concentration and its $\delta^{13}C$, and a 0.5-m-long section with water for analysis of chloride and sulfate concentration. Near the end of the 300-m-long coil attached to the BW-OS, the salinities changed from brackish values (2–3 psu) to fresh (0 psu), indicating the end of the sample record. Based on pumping rates, each 4.5-m section represents 1.8 days for the FW-OS and 2.9 days for the BW-OS. Consequently, it was possible to ascribe a time interval to each section of the coil. Sample water from the 4 m copper tubing sections was expelled into 10-ml syringes using a benchtop tube roller and a gas tight connection between the tubing and syringe. Out of the 192 samples extracted, 34 were prepared for coupled methane concentration and $\delta^{13}C$-CH_4 analysis. These subsamples were extracted as described above with the modification that the sample was expelled into two 5-ml syringes connected with stopcocks.

2.4. Geochemical Analyses

Analyses were performed at the Woods Hole Oceanographic Institution and U.S. Geological Survey in Woods Hole, MA, USA. Methane concentrations were determined by injecting 3-ml headspace directly from the syringe into a Shimadzu 14-A gas chromatograph equipped with a flame ionization detector. The gases were isothermally (50 °C) separated with a Poraplot-Q stainless steel column (2.44 m × 3.18 mm outer diameter) packed with 60/80 mesh and quantified against certified gas standards with a relative standard deviation of 2.8% or less. Headspace concentrations were converted to dissolved concentrations following established methods (Magen et al., 2014).

The $\delta^{13}C$ signature of methane in the headspace of the syringe was determined using an Isotope-ratio-monitoring gas chromatography-mass spectrometry system consisting of an Agilent 6890 Gas Chromatograph coupled to a Thermo-Finnigan DELTA^{Plus} XL isotope-ratio mass spectrometer through a Finnigan GCCIII combustion interface held at 1080 °C with a constant oxygen trickle. The gas sample was introduced directly from the 2-ml headspace in the syringe through a gas sampling valve into a He carrier gas stream. Methane and other condensable gases were trapped on a fused silica capillary packed with 80/100 mesh Poraplot-Q immersed in liquid nitrogen modified after Popp et al. (1995). The gases were thermally desorbed from the packing at 200 °C and separated on a 30-m, 0.32-mm ID Poraplot-Q column, oxidized to CO_2, and analyzed by Isotope-ratio Mass Spectrometry. The $^{13}C/^{12}C$ ratios of methane were expressed in the standard δ-notation using tank CO_2 referenced to the Vienna Pee Dee Belemnite standard. The standard deviation (1 σ) of a 1% CH_4 standard analyzed at least every eight samples was 0.3‰.

Sulfate and chloride concentrations were determined using a Metrohm 881 Compact Plus ion chromatograph equipped with a Metrosep A Supp 5-250 anion column. Samples from the FW and BW were diluted by factors of 31 and 61, respectively, to maintain the chloride peak within the limit of the conductivity detector. Peak areas for sulfate and chloride were quantified against equivalently diluted International Association for the Physical Sciences of the Oceans standard seawater analyzed at the beginning of the

run and after every fifth sample. Chloride concentrations (mM) were converted to mg/L and multiplied by 0.0018066 to determine salinity (psu). The analytical error for dissolved constituents was ±3.5% of the International Association for the Physical Sciences of the Oceans standard sulfate and chloride values. Measured sulfate and chloride concentrations were reported in related data release (Brankovits et al., 2018).

2.5. Statistical Analyses

Wavelet analysis using precipitation, water level, and water velocity was conducted to identify intervals of coherence and phase lags between the hydrologic parameters. The analysis was performed following the methods described by Grinsted et al. (2004). Cross wavelet transforms of two time series identify common power in time-frequency space, allowing for a mechanistic link between processes (Grinsted et al., 2004) and have been useful for identifying hydrologic mixing mechanisms and their temporal extent in unconfined aquifers within the Yucatan coastal platform (Coutino et al., 2017; Kovacs et al., 2017). Coherence between continuous wavelet transforms are more informative than standard lagged correlation analyses because they account for dynamic variations in time-frequency space. For example, the correlation between precipitation and water level may vary in terms of magnitude and phase as a function of the magnitude of the precipitation event.

Regression analysis was used to determine relationships between hydrologic and chemical records. Mean monthly values were used to minimize the effect of phase lags among the measured parameters (Gondwe et al., 2010; Kovacs et al., 2017). Furthermore, using mean monthly values made it possible to incorporate salinity and methane data from the chemical records where dates determined from OS pumping rates are subject to greater uncertainty at shorter time intervals than sensor-based time series. Linear regression analysis was performed on yearlong records collected on the surface (precipitation), in the FW (methane concentration and salinity), and in the BW (flow velocity).

2.6. Richardson Number

Density gradient stability was estimated at the two haloclines (H1 and H2) to investigate mixing. The gradient Richardson number, a ratio of the stabilizing density gradient to shear, can be calculated as

$$Ri = -\frac{g}{\rho_0}\frac{\frac{\partial \rho}{\partial z}}{\left(\frac{\partial u}{\partial z}\right)^2}, \quad (1)$$

where g is the acceleration due to gravity, ρ_0 is the reference fluid density, $\partial\rho/\partial z$ is the fluid vertical density gradient, and $\partial u/\partial z$ is the vertical gradient in horizontal velocity (shear). At $Ri > 0.25$, density gradients are stable and mixing is inhibited, while at $Ri < 0.25$, stratification breaks down and mixing occurs (Geyer & Smith, 1987). Fluid density of the water masses (FW, BW, and SG) was determined based on existing salinity profiles (Figure 2), resulting in a density difference of 1.3 kg/m^3 at the FW-BW gradient (H1) and 25.0 kg/m^3 at the BW-SG gradient (H2).

3. Results

3.1. Meteorological Records

The rainfall record showed seasonal and subseasonal variations (Figure 3a) consistent with the regional weather patterns. Total annual precipitation measured at the meteorological station was 1,387 mm (dry season [158 mm] and wet season [1,228 mm]). From this time series, June to November are defined as the wet period and December to May as the dry period (monthly precipitation <60 mm and < 4% of annual rainfall in subsequent months; Kottek et al., 2006; Peel et al., 2007). Although July was functionally a dry month with 20-mm total precipitation, for continuity of the record, July is included in the wet season. Annual mean air temperature was 27.8 °C with January being the coldest month (23.7 °C in 2015 and 24.3 °C in 2016), and July (30.7 °C) and August (30.4 °C) being the two warmest months (Brankovits et al., 2018).

3.2. Hydrologic Records

In the BW, changes in water level and flow velocity occurred on subtidal and tidal (Figure S2) to seasonal scales (Figure 3a). Water level was ~14 cm below the annual average during February and March and > 26 cm above the annual average during October and November. Water flow in the BW was always toward the

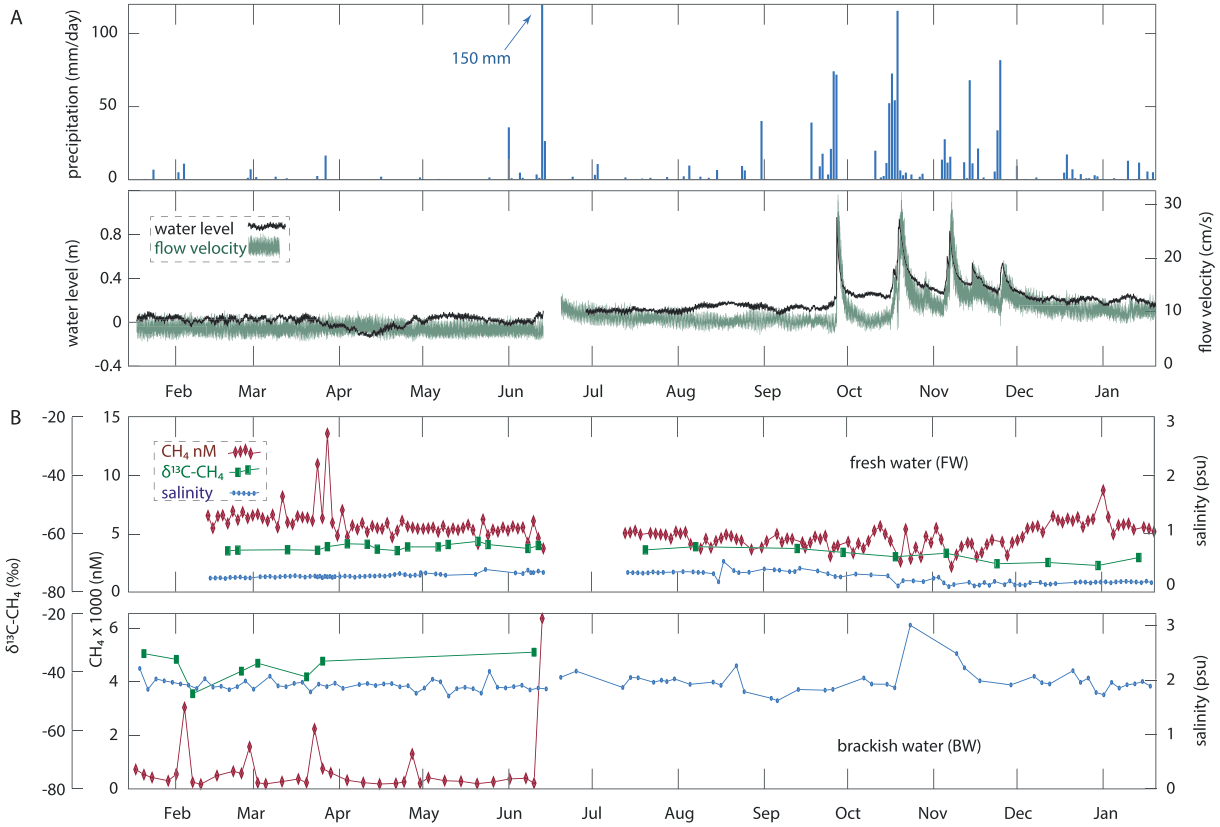

Figure 3. Precipitation, hydrologic, and chemical records from 15 January 2015 to 20 January 2016. (a) The precipitation record (upper) is plotted with water level and flow velocity (lower) from the brackish water (BW) where conduit flow is concentrated. (b) Chemical records from the FW (at 3.5-m water depth) and BW (at 7.5-m water depth) include methane concentrations (red diamond), δ^{13}C-CH_4 (green square), and salinity (blue circle).

coastline with velocities averaging 9.00 ± 0.01 cm/s during the yearlong deployment period, with lower and more stable velocity during the dry season (7.91 ± 0.01 cm/s) than during the rainy season (10.16 ± 0.01 cm/s). Episodic events with increased water level and velocity (up to 32.6 cm/s) occurred during the wet period (Figure 3).

The net saline groundwater (SG) flow was inland and opposite the seaward flowing BW. Measured flow velocity in the SG was, on average, 0.4 ± 0.1 cm/s during the yearlong deployment. These flow velocity values are below the reported detection limit of the tilt-current meter (Lowell et al., 2015), but are consistent with a previous study that suggested inland-flowing groundwater in conduits within the SG can explain temperature anomalies in the water column (Beddows et al., 2007).

3.3. Chemical Records

The OS deployed at 3.5 m in the FW (FW-OS) provided a 341-day chemical record (12 February to 14 June 2015 and 17 July 2015 to 19 January 2016) that includes a 29-day gap caused by overfilling the coils during the second deployment. Mean salinity during the yearlong deployment was 0.26 ± 0.01 psu in the FW. High methane concentrations (5,209 ± 102 nM) were observed year-round with a significantly ($p < 0.05$, t test) higher average value during the dry season (5,949 ± 132 nM) than during the wet season (4,361 ± 89 nM; Table 1). On five occasions, dry season methane concentrations exceeded 8,000 nM with a single event being greater than 13,500 nM (Figure 3). By contrast, the highest measured methane concentration in the wet season was 6,073 nM. Methane in the FW was characterized by depleted δ^{13}C values during the dry season (−65.2 ± 0.5‰) and the wet season (−65.8 ± 0.7‰; Table 1).

The BW-OS deployed at 7.5 m water depth in the BW provided a yearlong salinity record (19 January 2015 to 19 January 2016) with a 5-day gap between the end of the first deployment (14 June 2015) and the start of the second deployment. The first deployment resulted in a 151-day methane record (19 January 2015 to 14

Table 1
Summary of the Chemical Records From the Shallow Fresh Water (FW) and the Deeper Brackish Water (BW) Layers of the Meteoric Lens During the Dry (December to May) and Wet (June to November) Seasons

Record		Average CH_4 (nM)	Max. CH_4 (nM)	Min. CH_4 (nM)	$\delta^{13}C$-CH_4 (‰)	Salinity (psu)
Shallow FW	Dry season	5,949 ± 132 (86)	13,551	4,093	−65.2 ± 0.5 (17)	0.24 ± 0.01 (77)
	Wet season	4,361 ± 89 (75)	6,073	2,165	−65.8 ± 0.7 (9)	0.28 ± 0.01 (57)
	Full record	5,209 ± 102 (161)	13,551	2,165	−65.4 ± 0.4 (26)	0.26 ± 0.01 (134)
Deeper BW	Dry season	216 ± 34 (28)[a]	2,892	27	−38.8 ± 1.8 (7)	1.92 ± 0.01 (65)
	Wet season	179 ± 57 (3)[a]	6,214	32	−33.2 (1)	1.98 ± 0.05 (26)
	Full record	213 ± 31 (31)[a]	6,214	27	−38.1 ± 1.7 (8)	1.94 ± 0.02 (91)

[a]Average methane values in the BW were calculated using baseline methane concentration values, which exclude the periodically measured extreme high methane concentration values.

June 2015) that primarily included dry months and the beginning of the wet season (Figure 3b). For the second deployment, only salinity values are reported. The BW had a higher average salinity (1.94 ± 0.02 psu) than the FW (0.26 ± 0.01 psu) during the yearlong deployment. The BW chemical record revealed generally low methane concentrations with an average value of 213 ± 31 nM (Table 1). This mean value does not include the five, extremely positive, methane concentration anomalies (Figure 3b). Four of these methane peaks, reaching values between 1,157 and 2,892 nM, occurred during the dry season and coincided with low-intensity rain events. The final methane peak in the record was also the highest methane concentration measured in this water layer (6,214 nM). This increase in methane in the BW coincided with a high-intensity rainfall event on 13 June 2015 that delivered 154 mm of precipitation and a sudden decrease in methane concentrations in the FW from ~5,000 to 3,724 nM. The mean stable carbon isotopic value of methane was, on average, −38.1 ± 1.7‰ in the BW.

3.4. Statistical Analyses and the Richardson Number

Wavelet analysis between precipitation and flow velocity resulted in maximum coherence for periods of 30–100 hr (1–4 days; Figure 4) and a phase lag (precipitation leading water velocity) averaging ~20 hr (data not shown). The high-precipitation events during October and November led to high coherence on the ~512-hr (21 days) timescale, likely due to increased frequency of precipitation events. Auxiliary information about the hydrologic conditions is provided by the results of the wavelet analysis between precipitation and water level, as well as between water level and velocity (Figures S3 and S4).

Correlation analysis, performed with monthly mean values, revealed that accumulation of methane in the shallow meteoric lens (FW) is inversely correlated with precipitation (Figure 5a; $r^2 = 0.48$) and flow velocity (Figure 5b; $r^2 = 0.31$). Solving for a range of layer thicknesses (0.2–0.6 m; Brankovits et al., 2017) and observed velocity differences yielded a map of Richardson numbers for the hydrodynamic regime (Figure 6). These calculations show that periods of increased flow velocity in the BW during the wet season were likely capable of breaking down stratification at the FW-BW gradient ($Ri < 0.25$ for H1 is within parameter space), causing intense mixing between the methane source regime (FW) and the oxidizing regime (BW). In contrast, the BW-SG gradient (or H2) is outside the parameter space ($Ri < 0.25$ for H2; Figure 6) and thus was always stable at the study site.

4. Discussion

A 12-month, ~2.5-day resolution record of methane concentrations from the meteoric FW portion of a flooded cave conduit within the Yucatan Peninsula carbonate platform reveals that methane is present in high concentrations (5,209 ± 102 nM; $n = 161$) within the shallow meteoric lens throughout the year. Furthermore, the stable carbon isotopic content of the methane (−65.4 ± 0.4‰; $n = 26$) is ^{13}C-depleted and constant throughout the record. This isotopic content is consistent with methane being derived from a microbial source (e.g., Whiticar, 1999) and supports the hypothesis that it was formed from microbial decomposition of tropical forest vegetation preceding its transport into the cave environment (Brankovits et al., 2017). By contrast, within the underlying BW, methane concentrations during the dry season were lower (216 ± 34 nM; $n = 28$) and relatively ^{13}C enriched (−38.8 ± 1.8‰; $n = 7$), which is consistent with

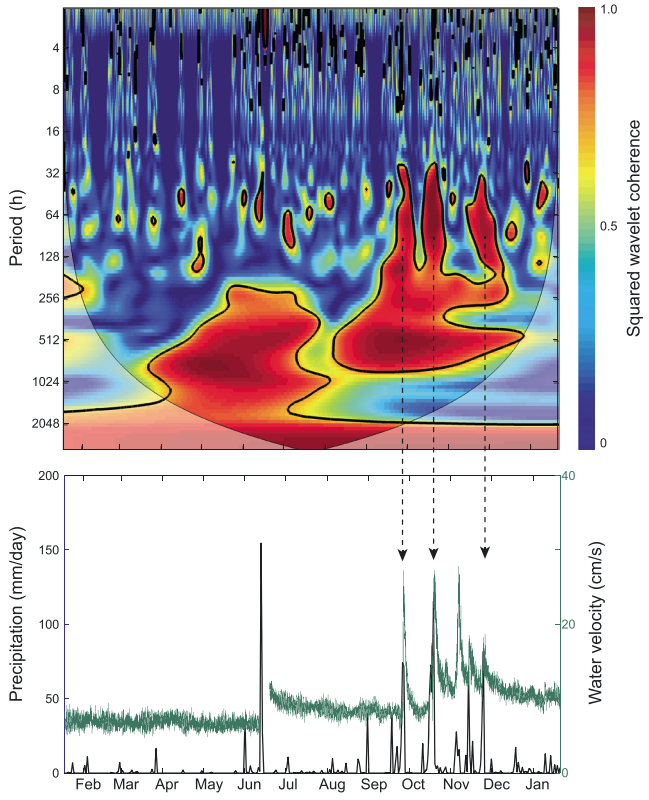

Figure 4. A comparison of wavelet coherence between precipitation and water velocity (upper), and a time series (lower) of precipitation (black lines) and water velocity (green lines). Coherence indicates that precipitation leads increase in flow velocity on varying timescales. Elevated coherence occurs during episodic, high-intensity precipitation events (arrows), with peak coherence varying with each event.

methane in the BW being residue from the FW after methane oxidation. These trends demonstrate that methane is available to the biological community throughout the year but that the microbial oxidation of methane requires mixing of the anoxic, methane-rich FW with the hypoxic BW.

Short-term and long-term changes in methane concentrations within the FW and BW reveal temporal dynamics in methane availability and consumption that we hypothesize are linked to the hydrology and meteorology of the platform. A comparison and analysis of methane dynamics within this KSE to coincidental hydrological records of groundwater salinity, flow velocity, and water level, and meteorological record of precipitation are used here to develop a landscape-level hydrobiogeochemical model and calculate a first-order estimate of the magnitude of the methane sink for this highly stratified groundwater system.

4.1. Temporal Methane Dynamics

Higher source methane concentration during the dry season (5,949 ± 132 nM; n = 86) in comparison to the wet season (4,361 ± 89 nM; n = 75; Table 1; Figure 3b) suggests that periods of high precipitation limit methane accumulation in the anoxic shallow meteoric lens (FW). The seasonally varying methane concentrations are characterized by uniform ^{13}C-depleted values (−65.2 ± 0.5‰ in dry and − 65.8 ± 0.7‰ in wet period), indicating a common, year-around active methane source produced by methanogenic microbes (e.g., Whiticar, 1999). The consistency of the values suggests methane oxidation, a process that enriches the ^{13}C content of the residual methane (Barker & Fritz, 1981), is not active within the FW.

The methane record from the BW was characterized by generally low concentrations (213 ± 31 nM) with five positive concentration anomalies (Figure 3b). Excess methane during these discrete events was most likely transported from the anoxic-FW, the only place where similarly high methane concentrations have been observed (Brankovits et al., 2017). The greatest methane concentration was recorded during a ~2.5-day period and was associated with the highest daily rainfall in the wet season. This event also coincided with the lowest methane concentration (3,724 nM) measured in the shallow meteoric lens during the first deployment period. The other four episodic methane peaks in the BW correspond with four low-intensity (2–17 mm/day) precipitation events in the dry season, suggesting that local rainfall is a plausible explanation for rapid methane input from the methane-charged shallow groundwater (FW) to the deeper portions of the meteoric lens (BW). Precipitation events not associated with methane peaks in the deeper meteoric lens are not likely to have been sufficiently intense to cause mixing between the FW and BW. Methane concentrations returned to baseline values less than 2.5 days after the mixing event (Figure 3). Removal by groundwater transport and/or biological consumption by methanotrophy are reasonable explanations for the rapid removal. Given the hypoxic conditions in the BW (Brankovits et al., 2017), it is most likely that the methane mixed into the BW is rapidly consumed by aerobic methanotrophs (e.g., Leonte et al., 2017; Steinle et al., 2015, 2017), resulting in the observed residual methane concentrations (216 ± 34 nM) with relatively enriched δ^{13}C values in the BW (−38.8 ± 1.8‰).

4.2. Links Between Water Chemistry, Hydrology and Meteorology

Wavelet and correlation analyses of the meteorology, hydrology, and water chemistry reveal that precipitation-induced effects in the groundwater hydrology facilitate mixing, transport, and consumption of methane. Water level leading flow velocity and positive relationships between tidal change and precipitation are well-known characteristics of unconfined carbonate aquifers (Beddows et al., 2002; Kovacs et al., 2017; Menning et al., 2015; Moore et al., 1992) that also occur in the KSE we investigated (Figures 4 and S3 and S4). For example, wavelet coherence between rainfall and water velocity indicates that precipitation

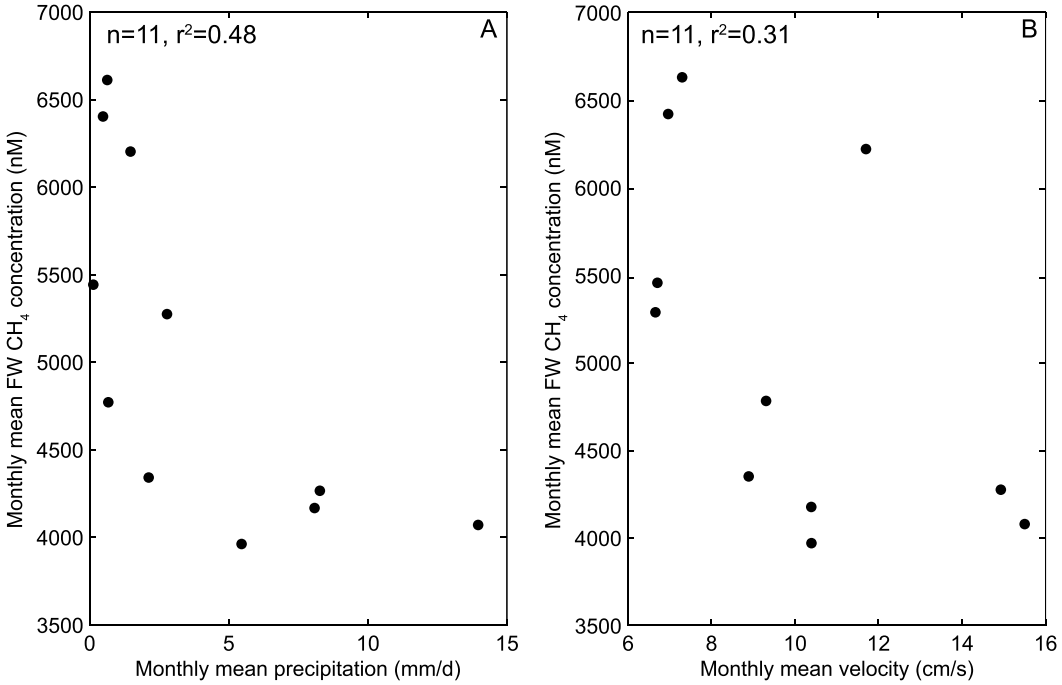

Figure 5. Relationships between methane concentrations and hydrology: monthly mean methane concentration in the fresh water (FW) is plotted with (a) mean precipitation; and (b) mean flow velocity in the brackish water (BW). Higher monthly mean precipitation and groundwater flow velocity correspond with lower methane concentrations, demonstrating that the local meteorology and aquifer hydrology affects methane accumulation in the karst subterranean estuary.

positively affects flow velocity for 1–4 days during small rainfall events and for up to 21 days during high-frequency, high-intensity precipitation events (Figure 4). Furthermore, methane concentration in the FW is inversely correlated with precipitation (Figure 5a; $r^2 = 0.48$) and flow velocity (Figure 5b; $r^2 = 0.31$). These relationships indicate that during precipitation events methane is either diluted by recharging meteoric water, mixed into the BW, produced at a lower rate, or some combination of these.

Material exchange between methane's source and oxidizing regimes (i.e., FW and BW, respectively) is important because it promotes methane oxidation. The potential for intense mixing at the FW-BW gradient (H1) is supported by the results of the Richardson number calculations that show stratification between FW and BW has the potential to break down ($Ri < 0.25$ for H1) during wet season high-flow events (Figure 6). The tendency for Ri to stay close or above the 0.25 threshold (Geyer et al., 2017) suggests that layers thicken in response to added shear in the wet season, and extensive mixing between the FW and BW is possible only under the highest observed velocities. Significantly ($p < 0.05$, t test) higher FW-salinity in the wet season than in the dry season (Table 1) further supports the idea that FW mixes with BW during the periods of increased precipitation.

Slightly higher BW salinity in the wet season than in the dry season (Table 1) and exceptionally elevated BW salinity measurements following frequent rainfalls in late October (Figure 3a) support the idea that salinity in the BW increases after rain-induced hydrological changes. This effect is a result of greater shear at the deeper halocline between the dynamic meteoric lens (with increased flow) and the more stagnant saline groundwater (Coutino et al., 2017; Kovacs et al., 2017). However, the fact that the BW-SG halocline (H2) was always stable during the sampling period (Figure 6; $Ri < 0.25$ for H2 is outside of parameter space) suggests mixing between the BW and SG primarily occurs upstream of the sampling station under a different mixing regime within caves or perhaps at cenotes containing saline groundwater (Coutino et al., 2017).

The evidence discussed above shows that the chemical composition of the anoxic, methane-charged shallow meteoric lens is susceptible to dilution of vertically recharging meteoric water and local mixing with the underlying BW layer. By contrast, the chemical composition of the methane-depleted BW is affected more

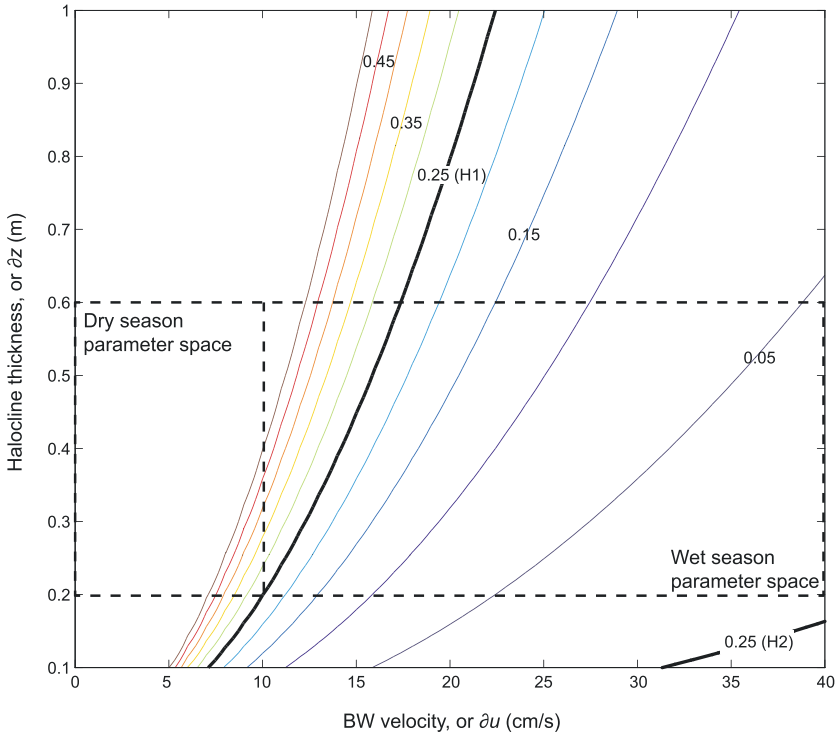

Figure 6. Richardson numbers for the haloclines. Contours of gradient Richardson number values as a function of halocline thickness (∂z) and velocity (∂u) in the BW; assuming FW and SG velocities are zero. FW-BW transition (H1) and BW-SG transition (H2). Intense mixing is expected at $Ri < 0.25$, suggesting that mixing between the FW and BW is more vigorous during the wet season. Range of thicknesses correspond to 0.2- and 0.6-m bounds reported by Brankovits et al. (2017); range of velocities in the BW correspond to ~10-cm/s peak velocity in dry season, and peak wet season velocities of >30 cm/s, as measured. BW = brackish water; FW = fresh water; SG = saline groundwater.

by vertical and horizontal inputs, allowing flow-induced mixing with the underlying saline groundwater to distribute salinity into the BW throughout the aquifer. These mixing dynamics are also relevant to water quality issues faced by ancient civilizations (Curtis et al., 1996; van Hengstum et al., 2010) as well as communities that currently depend on this resource (Bauer-Gottwein et al., 2011).

4.3. Magnitude of the Methane Sink Within the Subterranean Estuary

Simultaneous records of salinity and methane concentrations from the shallow and deeper portions of the meteoric lens obtained during the dry season (12 February 2015 to 31 May 2015) are used in a mixing model to determine the quantity of methane consumed in the KSE. These calculations are integrated with a hydrological model to provide a first-order estimate of methane consumption rates (MCRs) in the inland subterranean estuary.

The MCR within the drainage basin of the subterranean estuary investigated is expressed as

$$MCR_{\text{area}} = \frac{MCR_{\text{int}}}{A_{\text{SDB}}}, \tag{2}$$

where MCR_{area} is the MCR on an areal basis (mg $CH_4 \cdot m^{-2} \cdot year^{-1}$), MCR_{int} is the integrated MCR (mg CH_4/year), and A_{SDB} is the effective area (m^2) of the subterranean drainage basin.

The subterranean drainage basin area (A_{SDB}) is the surface area of the platform required to supply the measured volume of water flowing through the main passage of the cave during the studied time period and is calculated as

$$A_{\text{SDB}} = \frac{Q_{\text{BW}}}{\text{NIR}}, \tag{3}$$

where Q_{BW} is the mean volumetric flow (m^3/s) in the BW during the study period, and NIR is the net infiltration rate (m/s) of meteoric water into the aquifer, calculated as the difference between contributions from precipitation and losses by evapotranspiration and surface runoff. Because surface runoff in Quintana Roo, the location of the study site, is negligible (Beddows et al., 2007; Gondwe et al., 2010; Perry et al., 2002), NIR is expressed as the difference between average precipitation and evapotranspiration. Taking into account losses due to evapotranspiration, Gondwe et al. (2010) estimate that 17–23% of the mean annual precipitation infiltrates aquifers of the Yucatan Peninsula. Assuming a similar recharge efficiency and using precipitation rates of 3.75 mm/day or 4.34×10^{-8} m/s measured during this study, we estimate the NIR is between 7.38×10^{-9} and 9.98×10^{-9} m/s.

The Q_{BW}, or mean volumetric conduit flow through the BW (m^3/s), is calculated as

$$Q_{BW} = u \times A_{BW}, \tag{4}$$

where u is the average current velocity (m/s) within the BW, and A_{BW} is the average cross-sectional area (m^2) of the portion of the cave conduit that contains the BW.

Average current velocity (u) is estimated from a point measurement of flow velocity in the BW. The tilt-current meter deployed at ~17-m water depth measured flow velocity in the high-flow portion of the BW regime (near the midpoint of the cross-section), not accounting for expected disparity in water velocity distribution across the passage. However, velocity distribution within a cave conduit varies between subregimes of maximum and minimum velocity. Subregimes with the lowest flow are often close to zero velocity, and they can make up a substantial portion of the conduit cross section (Beddows, 2004). To account for the minimal flow subregimes within BW, the actual water velocity measurements during the study period (0.068 m/s, on average) are averaged with the expected minimal flow regimes (0 m/s) to get a conservative estimate of the mean water velocity (u = 0.034 m/s) across the passage.

To determine A_{BW}, or the average cross-sectional area of the BW (m^2), the following equation is used:

$$A_{BW} = A_{conduit} \times f_{BW}, \tag{5}$$

where $A_{conduit}$ is the full cross-sectional area of the passage (33.1 m^2) calculated based on estimated passage dimensions and f_{BW} is the fraction of the BW in the passage (0.9) based on the known position of haloclines within the conduit (Figures 2 and S5), which results in A_{BW} = 30 m^2. Only the flowing-BW fraction of the conduit's cross-sectional area is used for the calculation, because zero flow velocity, and therefore zero transport and consumption, is assumed for the top FW and the bottom SG. This assumption is based on the geomorphically protected nature of the shallow meteoric lens (Figure S1), including the FW, and the velocity measurements in the saline groundwater.

Calculations based on equations (4) and (5) result in an estimated mean volumetric flow (Q_{BW}) in the BW of 1.02 m^3/s, which is in close agreement with reported discharge rates (0.76–0.96 m^3/s) from single passages in the region (Beddows, 2004). Nevertheless, we recognize these estimates are a crude estimation of the volumetric flow in the BW regime. Measuring actual evapotranspiration rates on the surface, or recording temporal halocline dynamics and mapping the full extent of the flow velocity distribution (e.g., Ganju et al., 2012) in the cross-sectional conduit will provide more accurate volumetric flow calculations for a more quantitative assessment of this model. Using equation (5), Q_{BW} (1.02 m^3/s) and the range of NIR values (7.38×10^{-9} to 9.98×10^{-9} m/s), we calculate that the effective area of the subterranean drainage basin (A_{SDB}) is between 1.02×10^8 and 1.38×10^8 m^2 (or 102 to 138 km^2). However, we emphasize that the geometry of the drainage basin is unconstrained. The area we report is simply the hypothetical land surface area exposed to recharging meteoric water that is required to accumulate the volume of water estimated to pass through the high-flow passage we investigated.

The integrated MCR (MCR_{int}) beneath the land surface overlying the subterranean drainage basin (mg CH_4/year) during the study period is calculated as

$$MCR_{int} = C_{ox} \times Q_{BW}, \tag{6}$$

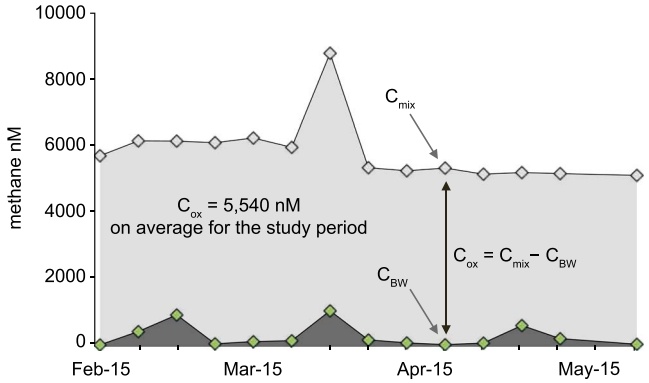

Figure 7. Calculation of methane oxidized for the study period in a weekly resolution. C_{mix} is the expected methane concentration in the BW if there was only physical mixing between water masses, based on the conservative mixing model. C_{BW} is the methane concentration actually measured in BW. C_{ox} is the amount of methane removed by oxidation, which is calculated to be 5,540 nmol/L (or 90.6 mg/m^3) indicating that, on average, 91% of source methane concentration is oxidized. The study period is 12 February to 31 May 2015.

where Q_{BW} (1.02 m^3/s converted to 3.23 × 10^{-8} m^3/year) is the volumetric flow and C_{ox} is the amount of methane consumed by methane oxidation (mg/m^3) in the system determined by conservative mixing calculations, a method that has been successfully applied in a variety of environments (Chanton & Lewis, 1999; Pohlman et al., 2008). C_{ox} is calculated as

$$C_{ox} = C_{mix} - C_{BW}, \quad (7)$$

where C denotes concentration of methane converted from nM to mg/m^3. C_{mix} is the expected methane concentration in BW if there was only physical mixing between water masses and C_{BW} is the methane concentration actually measured (Figure 7). C_{mix} is calculated as

$$C_{mix} = f_{FW}\, C_{FW} + (1 - f_{FW})\, C_{SG}, \quad (8)$$

where C_{FW} and C_{SG} are the endmember methane concentrations from the lowest (FW) and highest (SG) salinity regimes, respectively. The fraction of the fresh endmember (f_{FW}) present in the mixture is calculated from chloride concentrations as

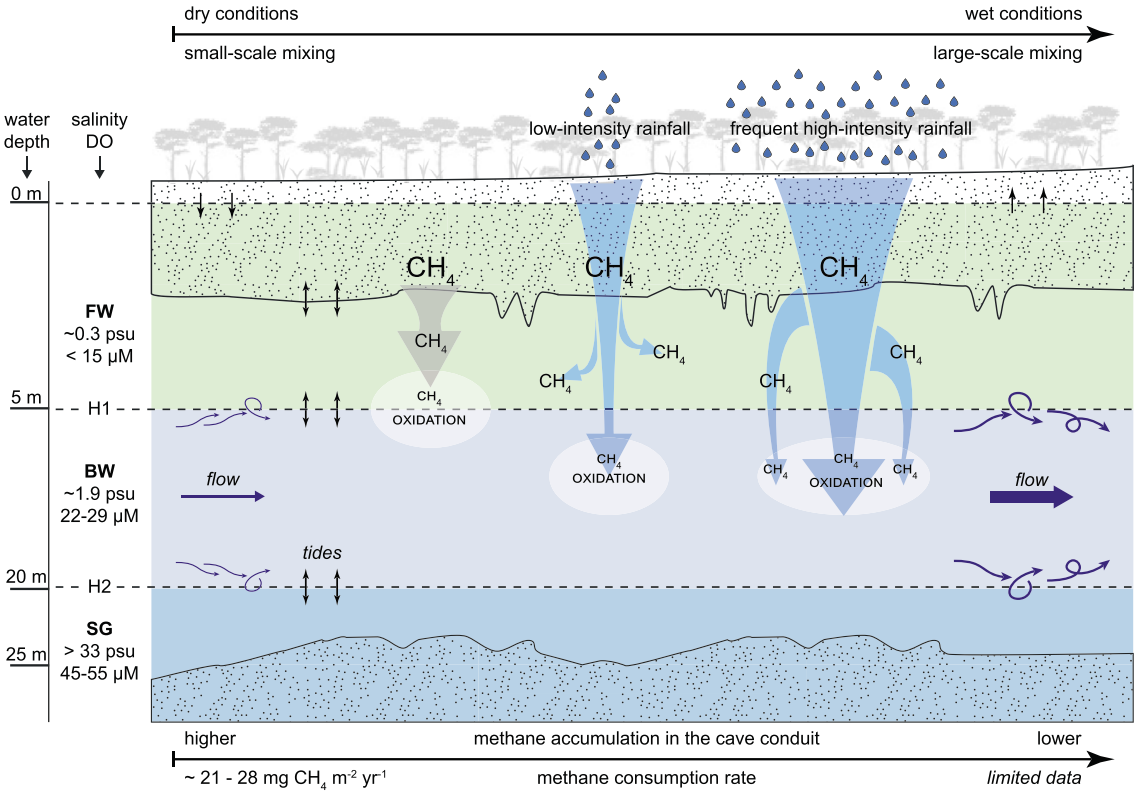

Figure 8. A conceptual model for seasonally influenced hydrologic regimes that govern methane dynamics in permanently flooded cave systems penetrating karst subterranean estuaries. The carbonate rock (dotted area) and the cave passages (plain area) are saturated below the groundwater table. The stratified groundwater consists of the meteoric lens, with layers of fresh water (FW) and brackish water (BW), and the saline groundwater (SG); water masses are separated by shallow (H1) and deep (H2) haloclines with differing dissolved oxygen concentrations (Brankovits et al., 2017). During dry periods, precipitation, flow and mixing are minimal. Methane accumulates in the anoxic FW (gray arrow), and its oxidation is restricted to the shallow halocline (H1). During low-intensity rainfall periods, methane accumulation in the FW continues (branched arrows terminate in FW); however, pulses of methane injected into the BW during rainfall events facilitate methane oxidation in the BW. During wet periods, frequent high-intensity rainfall creates an energetic mixing regime that drives more methane across H1, depletes methane in the FW, and increases methane oxidation in the BW (indicated by termination of branched arrows).

$$f_{FW} = \frac{[Cl^-]_{SG} - [Cl^-]_{mix}}{[Cl^-]_{SG} - [Cl^-]_{FW}}, \quad (9)$$

where $[Cl^-]$ denotes chloride concentration within the respective water mass (subscripts FW, BW, or SG). In this study, $[Cl^-]$ content is expressed as salinity (see section 2 for details), therefore, $[Cl^-]$ in equation (9) is substituted with salinity to determine f_{FW}.

For the above calculations, methane concentration and salinity time series records obtained from FW and BW are averaged for the study period within the representative water mass for each chemical property, resulting in values of 6,126 ± 268 nM for C_{FW}, 286 ± 91 nM for C_{BW}, 0.27 ± 0.01 psu for FW salinity, and 1.89 ± 0.01 psu for BW salinity. For the SG, reported values of average salinity (SG salinity = 32.84 ± 0.94 psu) and methane concentration (C_{SG} = 110 ± 17 nM) are used (Brankovits et al., 2017). Using equation (7), it is calculated that the C_{ox}, or the amount of methane consumed within each m^3 of mixed water is 5,540,107 nmol (or 90.6 mg CH_4/m^3), which is 91% of the original methane content. Inserting C_{ox} (90.6 mg CH_4/m^3) into equation (6) indicates an integrated MCR (MCR_{int}) of 2.86×10^9 mg CH_4/year within the Cenote Bang drainage basin during the study period. Given the study was conducted in the dry season, which lasted 6 months in the year investigated, we calculate that the total mass of methane consumed in the dry season was 1.43×10^9 mg (1,430 kg). Inserting MCR_{int} and the minimum and maximum A_{SDB} values into equation (2), it is calculated that the rate of methane consumption within the drainage basin of the subterranean estuary, or MCR_{area}, is between 21 and 28 mg $CH_4 \cdot m^{-2} \cdot year^{-1}$. This rate is expected to be higher with the integration of wet season methane dynamics when mixing scenarios are more prevalent. Thus, we suggest the current assessment is a conservative estimate for oxidation rates in KSEs.

The lateral export of methane toward the coast from the passage we investigated was 0.41 kg CH_4/day during the 15-week study period in the dry season. This flux was calculated by multiplying the mean volumetric flow (Q_{BW} = 1.02 m^3/s, or 88,128 m^3/day) and the mean methane concentration measured in the BW (C_{BW} = 286 nM, or 4.6×10^{-6} kg/m^3). Because this passage is located ~8 km inland, the methane fluxing from this site would be subjected to further oxidation during transport to the coast and the water mass may accumulate additional methane from the FW. Therefore, this calculated value is a rough approximation of the potential methane flux into the coastal ocean. More detailed studies are required to constrain the downstream oxidation rates and mixing dynamics in the aquifer for an accurate estimate of the coastal groundwater methane discharge.

5. Conclusions

Methane dynamics in KSEs are impacted by small- and large-scale mixing that is driven by hydrological mechanisms linked to meteorological and tidal changes (Figure 8). The dry season is characterized by more stable conditions and less mixing between stratified water masses than the wet season. Extended dry periods with occasional low-intensity-precipitation limit mixing between anoxic (FW) and hypoxic (BW) water masses. Hydrological conditions during the dry season are favorable for methane accumulation in the FW and limit methane transport from the FW to the BW. Rates of methanotrophy and other DOM-assimilating biogeochemical process are expected to be minimal during this hydrologically quiescent period, because exchange of material between water masses is primarily limited to diffusion along concentration gradients in the stratified groundwater. During the rainy season, precipitation of increasing frequency and intensity raises the water level and groundwater flow velocity, which dilutes the shallow meteoric lens and enhances turbulent mixing between water masses. Decreasing methane concentrations in the FW are the result of dilution from precipitation and increased material exchange between water masses. The chemical composition of the BW is affected by vertical and lateral inputs, allowing flow-induced mixing with the underlying SG to increase its salinity, and potentially dissolved oxygen. Vigorous mixing scenarios are more prevalent during the wet season, suggesting greater exchange of electron donors and electron acceptors between anoxic and oxic waters. As a result, hydrological processes directly facilitate biogeochemical pathways and support aerobic oxidation of methane. Evidence for methane consumption contributes to the increasing lines of evidence that the quantity of methane expelled by submarine groundwater discharge along coastlines (Cable et al., 1996; Kim & Hwang, 2002) is controlled by biogeochemical processes within subterranean estuaries (Schutte et al., 2016). To develop a quantitative and predictive understanding of feedbacks between the

aboveground climate, coastal groundwater hydrology, and the exchange of methane and other ecologically relevant compounds between the terrestrial and coastal ecosystems requires further investigation.

The estimated MCR of 21 to 28 mg $CH_4 \cdot m^{-2} \cdot year^{-1}$ during the dry season for the catchment area of this subterranean estuary is about 1–2% of the rates calculated for a barrier island subterranean estuary (1,446 mg $CH_4 \cdot m^{-2} \cdot year^{-1}$; Schutte et al., 2016), 2–3% of rates described from pristine forest soils (1,050 mg $CH_4 \cdot m^{-2} \cdot year^{-1}$; Price et al., 2004), and about 0.15–0.20% of the oxidation rate determined for a mud volcano with active methane seepage (14,400 mg $CH_4 \cdot m^{-2} \cdot year^{-1}$; Niemann et al., 2006). Therefore, methane consumption in KSEs is not likely to be a significant portion of the global methane sink. Nevertheless, methane consumed by methanotrophic bacteria supplies energy to the food web in this energy-limited habitat resulting in cave-adapted shrimp specimens with, on average, 21% of methane-derived carbon in their biomass (Brankovits et al., 2017). Consequently, the estimated ~1.4 t of methane oxidized in the 6-month-long dry season over the drainage basin confirms that methane is a substantial resource for the ecosystem, suggesting that the ecological significance of this methane sink is most likely more important than its role as a global sink for methane.

Although our model is based on observations from a single KSE in the tropics, we hypothesize the hydrologic controls on methane dynamics observed here are fundamentally applicable to all KSEs found in other geographical locations. Similar KSE environments are widespread among the carbonate islands of the Caribbean region, the Bahamas, and Bermuda (Beddows et al., 2002; Kambesis & Coke, 2013; Mylroie et al., 1995). Florida's limestone platform, where methane also provides carbon and energy for the subterranean food web (Opsahl & Chanton, 2006), has a significant coastal aquifer system with extensive cave passages that influence hydro-biogeochemical processes (Menning et al., 2015). Additional KSEs are found along coastlines globally (Ford & Williams, 2013), many of them inhabited by the anchialine fauna (Iliffe & Kornicker, 2009). Further investigations at other locations will test similarities and deviations from the current conceptual model described in this study. We hypothesize that distance to the coast will affect the ratio of terrestrial to marine inputs of dissolved organic material. Surface vegetation and land use will likely impact methane production and inputs into KSEs. Local climate and sea level will affect stratification and mixing. Because dissolved organic carbon (DOC) concentrations follow methane concentrations (i.e., high DOC is associated with high methane) in the studied KSE (Brankovits et al., 2017), hydrological controls on methane dynamics have implications to predict DOC inputs as well. Our conceptual model provides baseline information on methane dynamics and carbon cycling for future investigations in other KSEs.

Acknowledgments
Funding for T. M. I. and D. B. was provided by TAMU-CONACYT (project 2015-049). D. B. was supported by the Research-in-Residence program (NSF award 1137336, Inter-university Training in Continental-scale Ecology), the Boost Fellowship (Texas A&M University at Galveston), and the Postdoctoral Scholar Program by Woods Hole Oceanographic Institution and U.S. Geological Survey. We thank Jacob Pohlman and István Brankovits for assistance with field expeditions. Special thanks to the late Bil Phillips (Speleotech) for the support and expertise provided us during field operations. We also thank Pete van Hengstum for productive discussions and guidance during the development of the manuscript. Michael Casso and Adrian Green helped with laboratory analyses. The manuscript was greatly improved by helpful comments from an anonymus reviewer, Jeff Chanton, and Meagan Gonneea. This work is contribution number UMCES 5541. Any use of trade names is for descriptive purposes and does not imply endorsement by the U.S. Government. The authors declare no competing financial interests. Archival data are available through the USGS ScienceBase-Catalog at https://doi.org/10.5066/P9U0KRVM.

References

Barker, J. F., & Fritz, P. (1981). Carbon isotope fractionation during microbial methane oxidation. *Nature*, *293*(5830), 289–291. https://doi.org/10.1038/293289a0

Bastviken, D., Cole, J., Pace, M., & Tranvik, L. (2004). Methane emissions from lakes: Dependence of lake characteristics, two regional assessments, and a global estimate. *Global Biogeochemical Cycles*, *18*, GB4009. https://doi.org/10.1029/2004GB002238

Bastviken, D., Ejlertsson, J., Sundh, I., & Tranvik, L. (2003). Methane as a source of carbon and energy for lake pelagic food webs. *Ecology*, *84*(4), 969–981. https://doi.org/10.1890/0012-9658(2003)084[0969:MAASOC]2.0.CO;2

Bauer-Gottwein, P., Gondwe, B. R., Charvet, G., Marín, L. E., Rebolledo-Vieyra, M., & Merediz-Alonso, G. (2011). The Yucatán Peninsula karst aquifer, Mexico. *Hydrogeology Journal*, *19*(3), 507–524. https://doi.org/10.1007/s10040-010-0699-5

Beddows, P., Smart, P., Whitaker, F., & Smith, S. (2002). Density stratified groundwater circulation on the Caribbean Coast of the Yucatan Peninsula, Mexico. *Karst Frontiers*. *Karst Waters Institute Special Publication*, *7*, 129–134.

Beddows, P. A. (2004). Groundwater hydrology of a coastal conduit carbonate aquifer: Caribbean coast of the Yucatán Peninsula, México. University of Bristol.

Beddows, P. A., Smart, P. L., Whitaker, F. F., & Smith, S. L. (2007). Decoupled fresh-saline groundwater circulation of a coastal carbonate aquifer: Spatial patterns of temperature and specific electrical conductivity. *Journal of Hydrology*, *346*(1-2), 18–32. https://doi.org/10.1016/j.jhydrol.2007.08.013

Bishop, R. E., Humphreys, W. F., Cukrov, N., Zic, V., Boxshall, G. A., Cukrov, M., et al. (2015). "Anchialine" redefined as a subterranenan estuary in crevicular or cavernous geological setting. *Journal of Crustacean Biology*, *35*(4), 511–514. https://doi.org/10.1163/1937240X-00002335

Brankovits, D., Pohlman, J. W., Mann, A. G., & Lapham, L. L. (2018). Temporal hydrologic and chemical records from the Ox Bel Ha cave network within the coastal aquifer of the Yucatan Peninsula, from January 2015 to January 2016. USGS ScienceBase Catalog. https://doi.org/10.5066/P9U0KRVM

Brankovits, D., Pohlman, J. W., Niemann, H., Leigh, M. B., Leewis, M.-C., Becker, K. W., et al. (2017). Methane-and dissolved organic carbon-fueled microbial loop supports a tropical subterranean estuary ecosystem. *Nature Communications*, *8*(1), 1835. https://doi.org/10.1038/s41467-017-01776-x

Cable, J. E., Bugna, G. C., Burnett, W. C., & Chanton, J. P. (1996). Application of 222Rn and CH4 for assessment of groundwater discharge to the coastal ocean. *Limnology and Oceanography*, *41*(6), 1347–1353. https://doi.org/10.4319/lo.1996.41.6.1347

Chanton, J. P., & Lewis, F. G. (1999). Plankton and dissolved inorganic carbon isotopic composition in a river-dominated estuary: Apalachicola Bay, Florida. *Estuaries*, *22*(3), 575–583. https://doi.org/10.2307/1353045

Coutino, A., Stastna, M., Kovacs, S., & Reinhardt, E. (2017). Hurricanes Ingrid and Manuel (2013) and their impact on the salinity of the Meteoric Water Mass, Quintana Roo, Mexico. *Journal of Hydrology*, *551*, 715–729. https://doi.org/10.1016/j.jhydrol.2017.04.022

Curtis, J. H., Hodell, D. A., & Brenner, M. (1996). Climate variability on the Yucatan Peninsula (Mexico) during the past 3500 years, and implications for Maya cultural evolution. *Quaternary Research*, *46*(01), 37–47. https://doi.org/10.1006/qres.1996.0042

Ford, D., & Williams, P. D. (2013). *Karst hydrogeology and geomorphology*. West Sussex, UK: John Wiley.

Ganju, N. K., Hayn, M., Chen, S.-N., Howarth, R. W., Dickhudt, P. J., Aretxabaleta, A. L., & Marino, R. (2012). Tidal and groundwater fluxes to a shallow, microtidal estuary: Constraining inputs through field observations and hydrodynamic modeling. *Estuaries and Coasts*, *35*(5), 1285–1298. https://doi.org/10.1007/s12237-012-9515-x

Gelesh, L., Marshall, K., Boicourt, W., & Lapham, L. (2016). Methane concentrations increase in bottom waters during summertime anoxia in the highly eutrophic estuary, Chesapeake Bay, USA. *Limnology and Oceanography*, *61*(S1), S253–S266. https://doi.org/10.1002/lno.10272

Geyer, W. R., Ralston, D. K., & Holleman, R. C. (2017). Hydraulics and mixing in a laterally divergent channel of a highly stratified estuary. *Journal of Geophysical Research: Oceans*, *122*, 4743–4760. https://doi.org/10.1002/2016JC012455

Geyer, W. R., & Smith, J. D. (1987). Shear instability in a highly stratified estuary. *Journal of Physical Oceanography*, *17*(10), 1668–1679. https://doi.org/10.1175/1520-0485(1987)017<1668:SIIAHS>2.0.CO;2

Gondwe, B. R., Lerer, S., Stisen, S., Marín, L., Rebolledo-Vieyra, M., Merediz-Alonso, G., & Bauer-Gottwein, P. (2010). Hydrogeology of the south-eastern Yucatan Peninsula: New insights from water level measurements, geochemistry, geophysics and remote sensing. *Journal of Hydrology*, *389*(1-2), 1–17. https://doi.org/10.1016/j.jhydrol.2010.04.044

Gonneea, M. E., Charette, M. A., Liu, Q., Herrera-Silveira, J. A., & Morales-Ojeda, S. M. (2014). Trace element geochemistry of groundwater in a karst subterranean estuary (Yucatan Peninsula, Mexico). *Geochimica et Cosmochimica Acta*, *132*, 31–49. https://doi.org/10.1016/j.gca.2014.01.037

Grinsted, A., Moore, J. C., & Jevrejeva, S. (2004). Application of the cross wavelet transform and wavelet coherence to geophysical time series. *Nonlinear Processes in Geophysics*, *11*(5/6), 561–566. https://doi.org/10.5194/npg-11-561-2004

He, R., Wooller, M. J., Pohlman, J. W., Tiedje, J. M., & Leigh, M. B. (2015). Methane-derived carbon flow through microbial communities in arctic lake sediments. *Environmental Microbiology*, *17*(9), 3233–3250. https://doi.org/10.1111/1462-2920.12773

Iliffe, T. M., & Kornicker, L. S. (2009). Worldwide diving discoveries of living fossil animals from the depths of anchialine and marine caves. *Smithsonian Contributions to the Marine Sciences*, *38*, 269–280.

Intergovernmental Panel on Climate Change (2014). *Climate change 2014—Impacts, adaptation and vulnerability: Regional aspects*. Cambridge, United Kingdom and New York, NY: Cambridge University Press.

Jannasch, H. W., Wheat, C. G., Plant, J. N., Kastner, M., & Stakes, D. S. (2004). Continuous chemical monitoring with osmotically pumped water samplers: OsmoSampler design and applications. *Limnology and Oceanography: Methods*, *2*, 102–113.

Kambesis, P. N., & Coke, J. G. (2013). *Overview of the controls on eogenetic cave and karst development in Quintana Roo* (pp. 347–373). Mexico: Coastal Karst Landforms. Springer.

Kim, G., & Hwang, D. W. (2002). Tidal pumping of groundwater into the coastal ocean revealed from submarine ^{222}Rn and CH_4 monitoring. *Geophysical Research Letters*, *29*(14), 1678. https://doi.org/10.1029/2002GL015093

Kottek, M., Grieser, J., Beck, C., Rudolf, B., & Rubel, F. (2006). World map of the Köppen-Geiger climate classification updated. *Meteorologische Zeitschrift*, *15*(3), 259–263. https://doi.org/10.1127/0941-2948/2006/0130

Kovacs, S. E., Reinhardt, E. G., Stastna, M., Coutino, A., Werner, C., Collins, S. V., et al. (2017). Hurricane Ingrid and Tropical Storm Hanna's effects on the salinity of the coastal aquifer, Quintana Roo, Mexico. *Journal of Hydrology*, *551*, 703–714. https://doi.org/10.1016/j.jhydrol.2017.02.024

Kwon, E. Y., Kim, G., Primeau, F., Moore, W. S., Cho, H. M., DeVries, T., et al. (2014). Global estimate of submarine groundwater discharge based on an observationally constrained radium isotope model. *Geophysical Research Letters*, *41*, 8438–8444. https://doi.org/10.1002/2014GL061574

Lapham, L., Wilson, R., Riedel, M., Paull, C. K., & Holmes, M. E. (2013). Temporal variability of in situ methane concentrations in gas hydrate-bearing sediments near Bullseye Vent, Northern Cascadia margin. *Geochemistry, Geophysics, Geosystems*, *14*, 2445–2459. https://doi.org/10.1002/ggge.20167

Lapham, L. L., Chanton, J. P., Martens, C. S., Higley, P. D., Jannasch, H. W., & Woolsey, J. R. (2008). Measuring temporal variability in pore-fluid chemistry to assess gas hydrate stability: Development of a continuous pore-fluid array. *Environmental Science & Technology*, *42*(19), 7368–7373. https://doi.org/10.1021/es801195m

Lee, Y. W., Kim, G., Lim, W. A., & Hwang, D. W. (2010). A relationship between submarine groundwater-borne nutrients traced by Ra isotopes and the intensity of dinoflagellate red-tides occurring in the southern sea of Korea. *Limnology and Oceanography*, *55*(1), 1–10. https://doi.org/10.4319/lo.2010.55.1.0001

Leonte, M., Kessler, J. D., Kellermann, M. Y., Arrington, E. C., Valentine, D. L., & Sylva, S. P. (2017). Rapid rates of aerobic methane oxidation at the feather edge of gas hydrate stability in the waters of Hudson Canyon, US Atlantic Margin. *Geochimica et Cosmochimica Acta*, *204*, 375–387. https://doi.org/10.1016/j.gca.2017.01.009

Levin, L. A. (2005). Ecology of cold seep sediments: Interactions of fauna with flow, chemistry and microbes. *Oceanography and marine biology: An annual review*, *43*, 1–46.

Lowell, N. S., Walsh, D. R., & Pohlman, J. W. (2015). A comparison of tilt current meters and an acoustic Doppler current meter in vineyard sound, Massachusetts. *Current, Waves and Turbulence Measurement* (CWTM), 2015 IEEE/OES eleventh. IEEE, pp. 1–7.

Magen, C., Lapham, L. L., Pohlman, J. W., Marshall, K., Bosman, S., Casso, M., & Chanton, J. P. (2014). A simple headspace equilibration method for measuring dissolved methane. *Limnology and Oceanogaphy: Methods*, *12*, 637–650.

Martin, J. B., Gulley, J., & Spellman, P. (2012). Tidal pumping of water between Bahamian blue holes, aquifers, and the ocean. *Journal of Hydrology*, *416*, 28–38.

Menning, D. M., Wynn, J. G., & Garey, J. R. (2015). Karst estuaries are governed by interactions between inland hydrological conditions and sea level. *Journal of Hydrology*, *527*, 718–733. https://doi.org/10.1016/j.jhydrol.2015.05.021

Moore, W. S. (1999). The subterranean estuary: A reaction zone of ground water and sea water. *Marine Chemistry*, *65*(1-2), 111–125. https://doi.org/10.1016/S0304-4203(99)00014-6

Moore, W. S. (2010). The effect of submarine groundwater discharge on the ocean. *Annual Review of Marine Science*, *2*(1), 59–88. https://doi.org/10.1146/annurev-marine-120308-081019

Moore, Y. H., Stoessell, R. K., & Easley, D. H. (1992). Fresh-water/sea-water relationship within a ground-water flow system, northeastern coast of the Yucatan Peninsula. *Groundwater*, *30*(3), 343–350. https://doi.org/10.1111/j.1745-6584.1992.tb02002.x

Mylroie, J. E., Carew, J. L., & Vacher, H. (1995). Karst development in the Bahamas and Bermuda. *Geological Society of America Special Papers*, *300*, 251–267.

Niemann, H., Linke, P., Knittel, K., MacPherson, E., Boetius, A., Bruckmann, W., Larvik, G., et al. (2013). Methane-carbon flow into the benthic food web at cold seeps—A case study from the Costa Rica Subduction Zone. *PLoS One*, *8*(10), e74894. https://doi.org/10.1371/journal.pone.0074894

Niemann, H., Losekann, T., de Beer, D., Elvert, M., Nadalig, T., Knittel, K., et al. (2006). Novel microbial communities of the Haakon Mosby mud volcano and their role as a methane sink. *Nature*, *443*(7113), 854–858. https://doi.org/10.1038/nature05227

Opsahl, S. P., & Chanton, J. P. (2006). Isotopic evidence for methane-based chemosynthesis in the Upper Floridan aquifer food web. *Oecologia*, *150*(1), 89–96. https://doi.org/10.1007/s00442-006-0492-2

Peel, M. C., Finlayson, B. L., & McMahon, T. A. (2007). Updated world map of the Köppen-Geiger climate classification. *Hydrology and Earth System Sciences Discussions*, *4*(2), 439–473. https://doi.org/10.5194/hessd-4-439-2007

Perry, E., Velazquez-Oliman, G., & Marin, L. (2002). The hydrogeochemistry of the karst aquifer system of the northern Yucatan Peninsula, Mexico. *International Geology Review*, *44*(3), 191–221. https://doi.org/10.2747/0020-6814.44.3.191

Pohlman, J. W. (2011). The biogeochemistry of anchialine caves: Progress and possibilities. *Hydrobiologia*, *677*(1), 33–51. https://doi.org/10.1007/s10750-011-0624-5

Pohlman, J. W., Ruppel, C., Hutchinson, D. R., Downer, R., & Coffin, R. B. (2008). Assessing sulfate reduction and methane cycling in a high salinity pore water system in the northern Gulf of Mexico. *Marine and Petroleum Geology*, *25*(9), 942–951. https://doi.org/10.1016/j.marpetgeo.2008.01.016

Popp, B. N., Sansone, F. J., Rust, T. M., & Merritt, D. A. (1995). Determination of concentration and carbon isotopic composition of dissolved methane in sediments and nearshore waters. *Analytical Chemistry*, *67*(2), 405–411. https://doi.org/10.1021/ac00098a028

Price, S. J., Sherlock, R. R., Kelliher, F. M., McSeveny, T. M., Tate, K. R., & Condron, L. M. (2004). Pristine New Zealand forest soil is a strong methane sink. *Global Change Biology*, *10*(1), 16–26. https://doi.org/10.1046/j.1529-8817.2003.00710x

Reeburgh, W. S. (2007). Oceanic methane biogeochemistry. *Chemical Reviews*, *107*(2), 486–513. https://doi.org/10.1021/cr050362v

Schutte, C. A., Wilson, A. M., Evans, T., Moore, W. S., & Joye, S. B. (2016). Methanotrophy controls groundwater methane export from a barrier island. *Geochimica et Cosmochimica Acta*, *179*, 242–256. https://doi.org/10.1016/j.gca.2016.01.022

Socki, R. A., Perry, E. C., & Romanek, C. S. (2002). Stable isotope systematics of two cenotes from the northern Yucatan Peninsula, Mexico. *Limnology and Oceanography*, *47*(6), 1808–1818. https://doi.org/10.4319/lo.2002.47.6.1808

Steinle, L., Graves, C. A., Treude, T., Ferre, B., Biastoch, A., Bussmann, I., et al. (2015). Water column methanotrophy controlled by a rapid oceanographic switch. *Nature Geoscience*, *8*(5), 378–382. https://doi.org/10.1038/ngeo2420

Steinle, L., Maltby, J., Treude, T., Kock, A., Bange, H. W., Engbersen, N., et al. (2017). Effects of low oxygen concentrations on aerobic methane oxidation in seasonally hypoxic coastal waters. *Biogeosciences*, *14*(6), 1631–1645. https://doi.org/10.5194/bg-14-1631-2017

Taniguchi, M., Burnett, W. C., Cable, J. E., & Turner, J. V. (2002). Investigation of submarine groundwater discharge. *Hydrological Processes*, *16*(11), 2115–2129. https://doi.org/10.1002/hyp.1145

van Hengstum, P. J., Reinhardt, E. G., Beddows, P. A., & Gabriel, J. J. (2010). Linkages between Holocene paleoclimate and paleohydrogeology preserved in a Yucatan underwater cave. *Quaternary Science Reviews*, *29*(19-20), 2788–2798. https://doi.org/10.1016/j.quascirev.2010.06.034

Vesper, D. J., Loop, C. M., & White, W. B. (2001). Contaminant transport in karst aquifers. *Theoretical and Applied Karstology*, *13*, 101–111.

Whiticar, M. J. (1999). Carbon and hydrogen isotope systematics of bacterial formation and oxidation of methane. *Chemical Geology*, *161*(1-3), 291–314. https://doi.org/10.1016/S0009-2541(99)00092-3

Wilson, R., Lapham, L., Riedel, M., Holmes, M., & Chanton, J. (2015). Observing methane hydrate dissolution rates under sediment cover. *Marine Chemistry*, *172*, 12–22. https://doi.org/10.1016/j.marchem.2015.03.004